Materials Today Energy 21 (2021) 100844

Contents lists available at ScienceDirect

Materials Today Energy

journal homepage: www.journals.elsevier.com/materials-today-energy/

Sensitive in-operando observation of Li and O transport in thin-film Li-ion batteries

Vairavel Mathayan [a, *], Kenji Morita [b], Bun Tsuchiya [c], Rongbin Ye [d], Mamoru Baba [d], Daniel Primetzhofer [a]

[a] Department of Physics and Astronomy, Uppsala University, Box 516, SE-75120 Uppsala, Sweden
[b] Department of Research, Nagoya Industrial Science Research Institute, 2F Noah Yotsuya Building, 1-13, Yotsuyatori, Chikusa-ku, Nagoya, 464-0819 Japan
[c] Faculty of Science and Technology, Meijo University, 1-501, Shiogamaguchi, Tempaku-ku, Nagoya, 468-8502 Japan
[d] Faculty of Science and Engineering, Iwate University, Ueta-4-3-5, Morioka, Iwate, 020-8551, Japan

ARTICLE INFO

Article history:
Received 22 June 2021
Received in revised form
13 August 2021
Accepted 14 August 2021
Available online 19 August 2021

Keywords:
Coincidence ERDA
In situ RBS
Li depth profiling
O depth profiling
Solid-state battery
Oxide cathode

ABSTRACT

Thin-film batteries often contain oxides in the anode, cathode, and electrolyte materials. In-operando methods capable of Li and O depth profiling are relevant for battery research to study, e.g. diffusion and trapping of constituents. Here, we demonstrate ion beam–based analytical methods with high depth resolution and sensitivity for depth profiling Li and O in thin-film batteries using 10 MeV Li and He ions. Simultaneous depth profiling of Li and O was performed using combined coincidence elastic recoil detection analysis and Rutherford backscattering spectrometry measurements in the battery with 8 MeV He ions, and the Li and O transport was measured in operando. Reversible Li transport was observed from the LMO anode to the NbO cathode on charging and vice versa during discharging. O transport was observed from the LMO anode to the NbO cathode on first charging with 3.5 V but was not observed on further charging and discharging of the battery. Our in-operando measurements allow direct and quantitative observation of Li and O transport during charge-discharge cycles for thin-film batteries.

1. Introduction

Liquid electrolytes as used in conventional Li-batteries are potentially hazardous because of the growth of lithium dendrites in the batteries, which leads to shorting, as well as the fact that these electrolytes are highly flammable. Thus, for safety reasons, the use of Li metal in conventional batteries is limited [1]. In contrast, all solid-state Li-ion batteries (ASSLB) are promising candidates for high density energy storage and wearable electronics which for safety reasons may outperform conventional Li-ion batteries which use a less stable liquid electrolyte [2]. Solid-state batteries may use electrolytes such as Li–S [3], Li–O [4], or Li-polymer [5]. Compared with other electrolytes, Li–O electrolytes are very stable at high temperatures, whereas other critical parts such as anode and cathode materials of ASSLB are also often metal oxides [6–8]. Altogether, Li and other light elements (O, S, Na) are important species transferred across electrolytes during operation in batteries or unintended overpotential. Thus, analyzing light element transport is highly relevant for improving battery design and performance [9,10].

Different depth profiling techniques have been used to directly measure the Li distribution, and Li transport has been measured by in-operando depth profiling techniques. A direct experimental assessment of Li depth profiles is, however, difficult because of the low atomic number of lithium, complicating detection by photon or electron-based techniques. Neutron depth profiling (NDP) [11], particle-induced gamma ray emission [12], and nuclear reaction analysis (NRA) [13] are methods that can provide in-operando Li depth profiling in solid-state batteries. However, NDP is only sensitive to ^{6}Li, and although it can feature high depth resolution and is virtually non-destructive, there is a lack of facilities around the world. Also NRA is isotope specific and has limited depth resolution, but instead ion beam–based techniques are more accessible. Conventional elastic recoil detection analysis (ERDA) methods enable in-operando Li depth profiling with very good Li depth resolution which is needed for ultrathin batteries [14–16]. Recently, the Li depth profiling and in-operando Li transport were demonstrated in thin-film batteries (TFBs) by coincidence

* Corresponding author.
E-mail address: vairavel.mathayan@physics.uu.se (V. Mathayan).

https://doi.org/10.1016/j.mtener.2021.100844

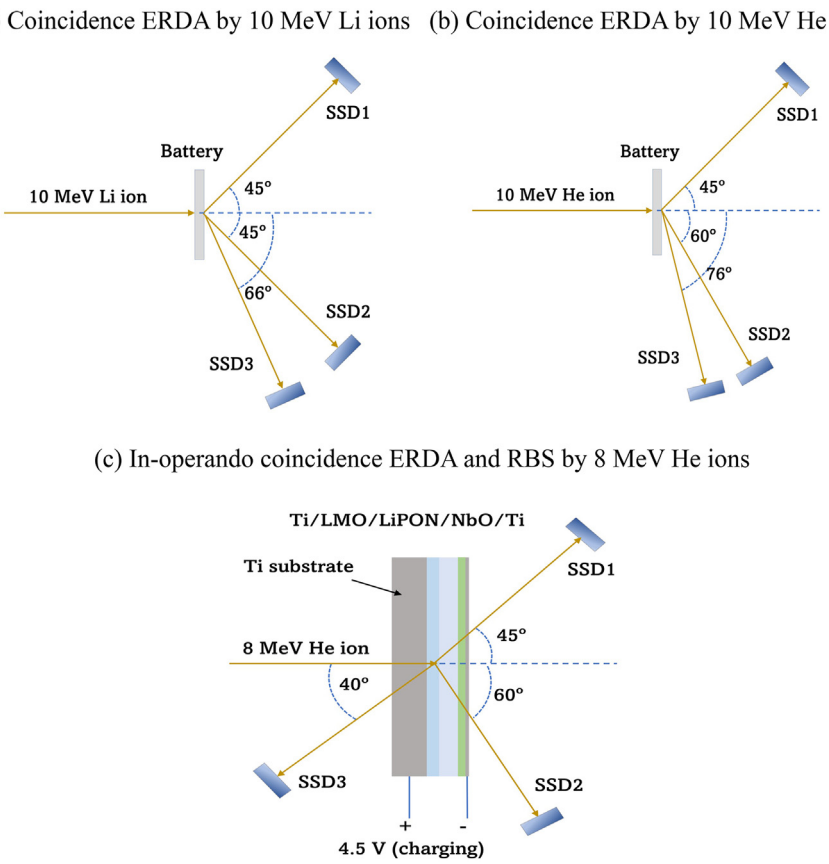

Fig. 1. Top view of the experimental setup used for simultaneous depth profiling of Li and O in the thin-film battery by coincidence ERDA using (a) 10 MeV Li ions and (b) 10 MeV He ions. (c) In-operando analysis of Li by coincidence ERDA (SSD1 and SSD2) and O by RBS (SSD3).

ERDA methods [17]. This approach provides very good depth resolutions for light elements, and the interaction of the probing beam with the sample can be used for simultaneous analysis of multiple light elements in thin samples.

In this study, we demonstrate simultaneous depth profiling of Li and O in a TFB stack by coincidence ERDA methods. Furthermore, we studied Li and O transport in the TFB by combining simultaneous measurements of coincidence ERDA and Rutherford backscattering spectrometry (RBS) during charge/discharge cycles.

2. Experimental details

The TFB used for the experiments features a LMO/LIPON/NbO/Ti layer structure on a Ti self-supporting foil mounted on a stainless steel frame [18]. Inclusion of H in the whole TFB stack is expected during sample preparation [19]. RBS was performed using 2 MeV He^{+} primary ions to determine the thickness of the Ti and NbO layer. NRA was performed by 2 MeV protons, and the total Li areal density in the TFB was determined from the yield of α particles from the $^{7}Li(p,\alpha)^{4}He$ nuclear reaction. In both RBS and NRA, the incident beam was directed toward the top Ti layer of the TFB in

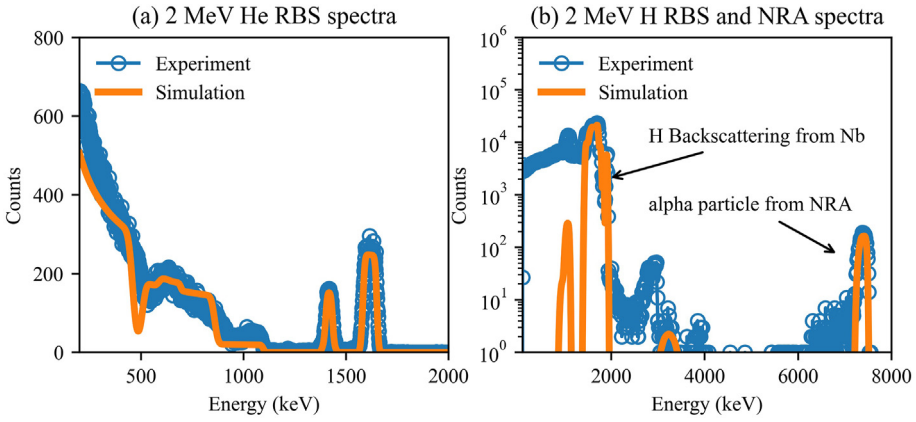

Fig. 2. (a) Experimental and simulated RBS spectra measured by 2 MeV He ions. (b) RBS/NRA spectra of the thin-film battery measured using 2 MeV $^{1}H^{+}$ ions in normal incidence to sample surface. The NRA spectra are normalized using scattered particles from Nb.

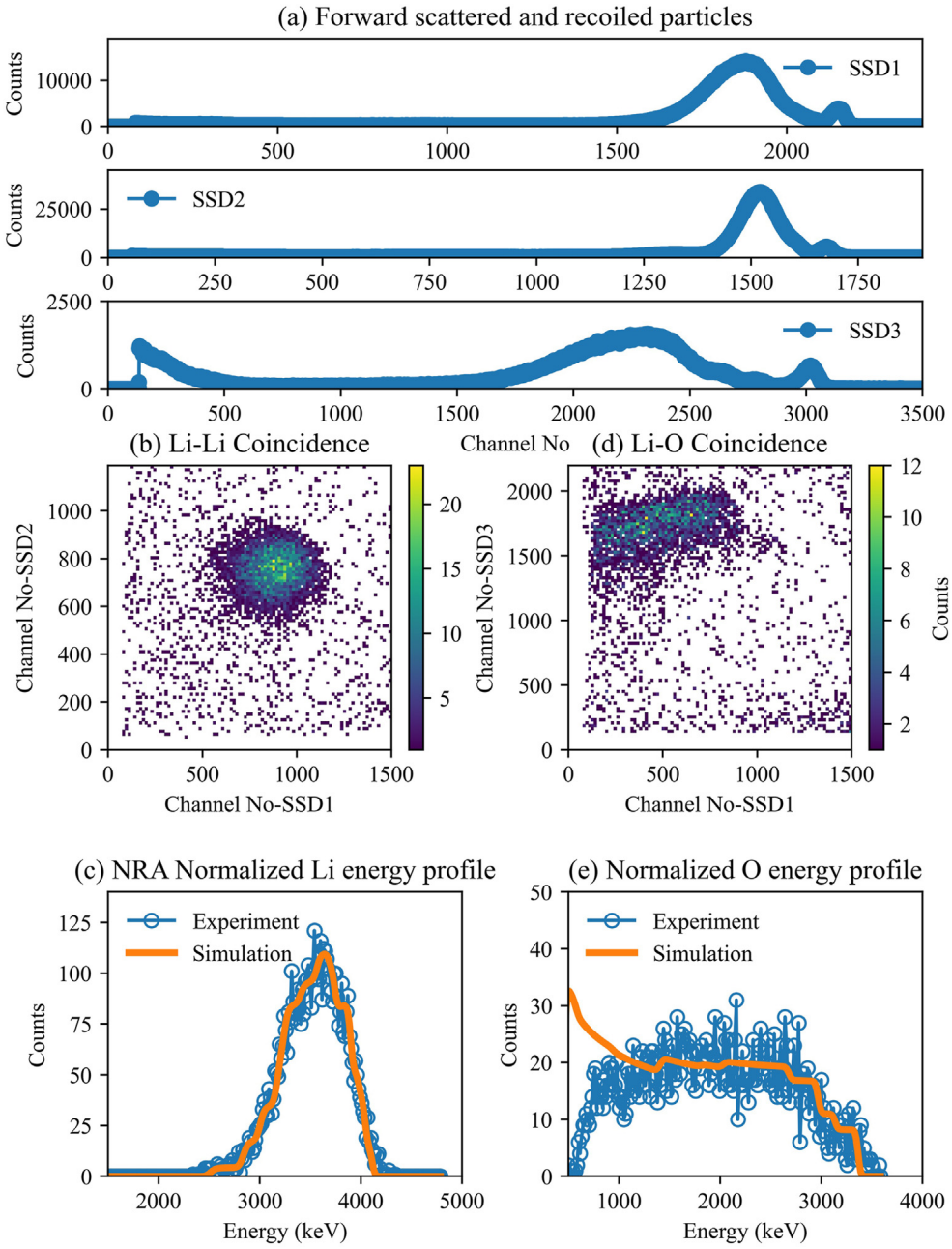

Fig. 3. (a) Experimental spectra of forward scattered/recoiled particles from the battery by 10 MeV $^{7}Li^{2+}$ ions. (b) Li–Li coincidence ERDA spectra of forward scattered/recoiled particles from two SSDs kept at 45°. (c) Experimental and simulated Li depth profile by Li–Li coincidence ERDA which is normalized by NRA. (d) Li–O coincidence ERDA spectra of forward scattered/recoiled particles from two detectors SSD1 and SSD3. (e) Experimental and simulated O depth profile by Li–Li coincidence ERDA.

normal incidence and the H/α particles were recorded using a silicon solid-state detector (SSD) with 20 keV energy resolution kept at an angle of 170° with respect to the incident beam. The RBS and NRA depth profiles were reconstructed by fitting the experimental spectra using the SIMNRA7.02 software [20]. Next, the coincidence ERDA technique was implemented using 10 MeV $^{4}He^{2+}$ and 10 MeV $^{7}Li^{2+}$ ions for specific detection of Li and O from the sample [21,22]. In these experiments, circular ion beams with 1 mm diameter were directed in normal incidence on the Ti substrate side of the TFB. For a primary beam of 10 MeV $^{7}Li^{2+}$, forward scattered ^{7}Li and recoiled ^{7}Li and ^{16}O were detected by SSD1, SSD2, and SSD3 kept at detection angles of 45°, 45°, and 66°, respectively, as shown in Fig. 1(a). The angle of SSD1 and SSD2 was chosen from trivial scattering kinematics [23], and Li–Li scattering events were recorded by coincidence of SSD1 and SSD2, whereas simultaneously Li–O scattering events were recorded by coincidence of SSD1 and SSD3. A coincidence time acceptance window of 1 μsec was used. The ion beam flux was set to approximately 5×10^{10} ions cm^{-2} s^{-1}. For 8 MeV $^{4}He^{2+}$-ions as the primary beam, scattered and recoiled Li and O were detected by SSD1, SSD2, and SSD3 with the scattering angle of 45°, 60°, and 76° (Fig. 1(b)). Again, a coincidence time acceptance window of 1 μsec was used, and He–Li and He–O scattering events were recorded from coincidence measurements of SSD1 with SSD2 and SSD3. The ion beam flux was set to approximately 5×10^{10} ions cm^{-2} s^{-1}. The detector resolution of all SSDs was approximately 20 and 25 keV for He and Li, respectively.

The in-operando Li and O depth profile was measured using 8 MeV He ions. Primary ions were again directed on the Ti substrate

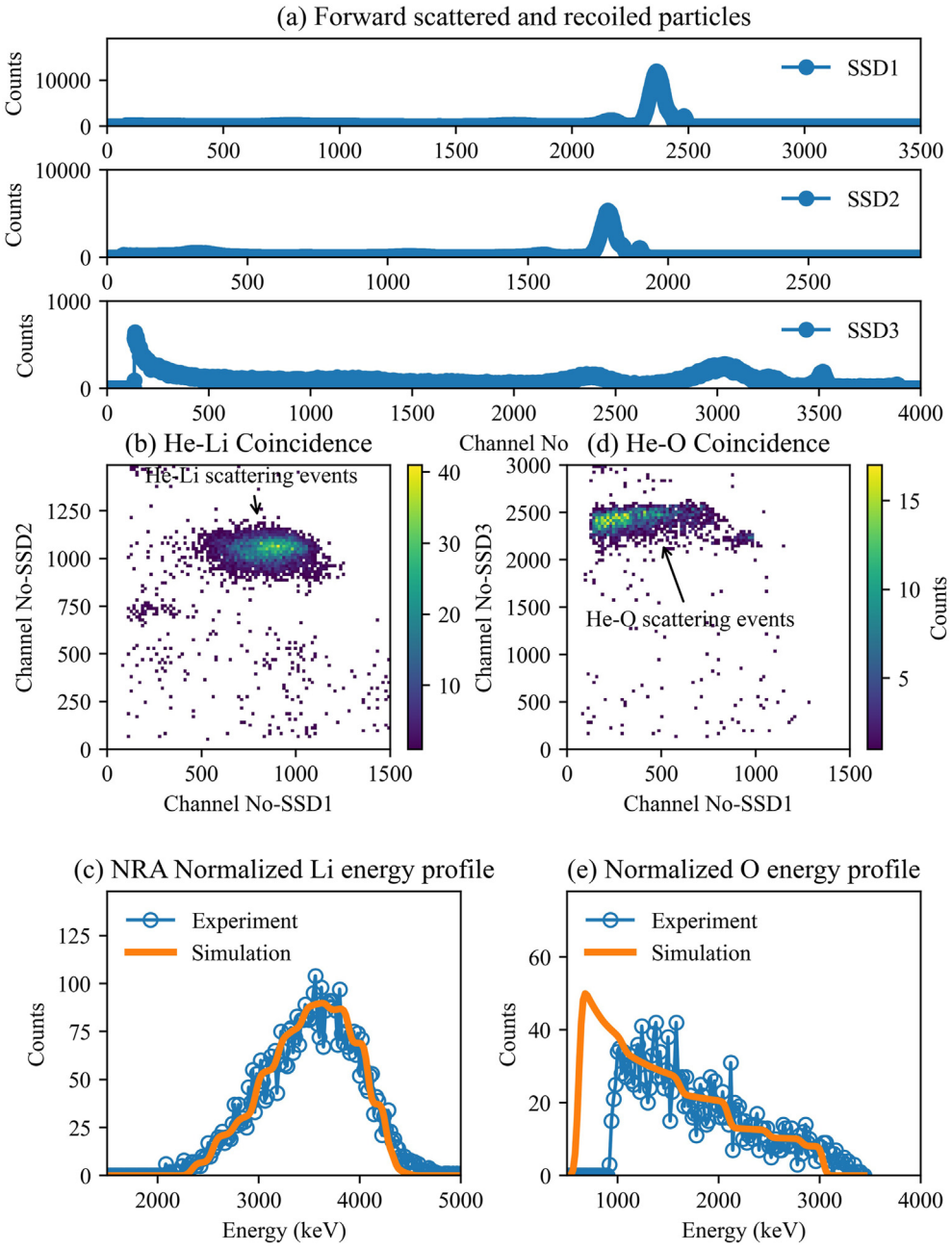

Fig. 4. (a) Experimental spectra of forward scattered/recoiled particles from the battery by 10 MeV He^{2+} ions. (b) He–Li coincidence ERDA spectra of forward scattered/recoiled particles from SSD1 and SSD2. (c) Experimental and simulated Li depth profile by He–Li coincidence ERDA which is normalized by NRA. (d) He–O coincidence ERDA spectra of forward scattered/recoiled particles from two detectors SSD1 and SSD3. (e) Experimental and simulated O depth profile by He–Li coincidence ERDA.

side, and the Li depth profile was measured using He–Li coincidence (SSD1 and SSD2 kept at 45° and 60° scattering angle), and the O profile was measured by RBS spectra simultaneously recorded by SSD3 at a backscattering angle of 140° (Fig. 1(c)). The Ti electrodes were connected to an external potentiostat to apply a well-defined electrical potential. The battery is charged by applying a positive potential to the bottom Ti substrate while the top Ti electrode was grounded. Then the positive potential was applied to the top Ti electrode for discharging.

3. Results and discussion

The experimental and simulated RBS spectra measured in TFB are shown in Fig. 2(a). From RBS, the thickness of Ti was found to be 300×10^{15} atoms/cm^2 and the composition and thickness of NbO were found to be $Nb_{0.34}O_{0.66}$ and 640×10^{15} atoms/cm^2, respectively. The NRA spectrum measured for the TFB is shown in Fig. 2(b). The resulting areal density of Li is 5350×10^{15} atoms/cm^2 in the whole battery stack. Altogether, thickness and composition

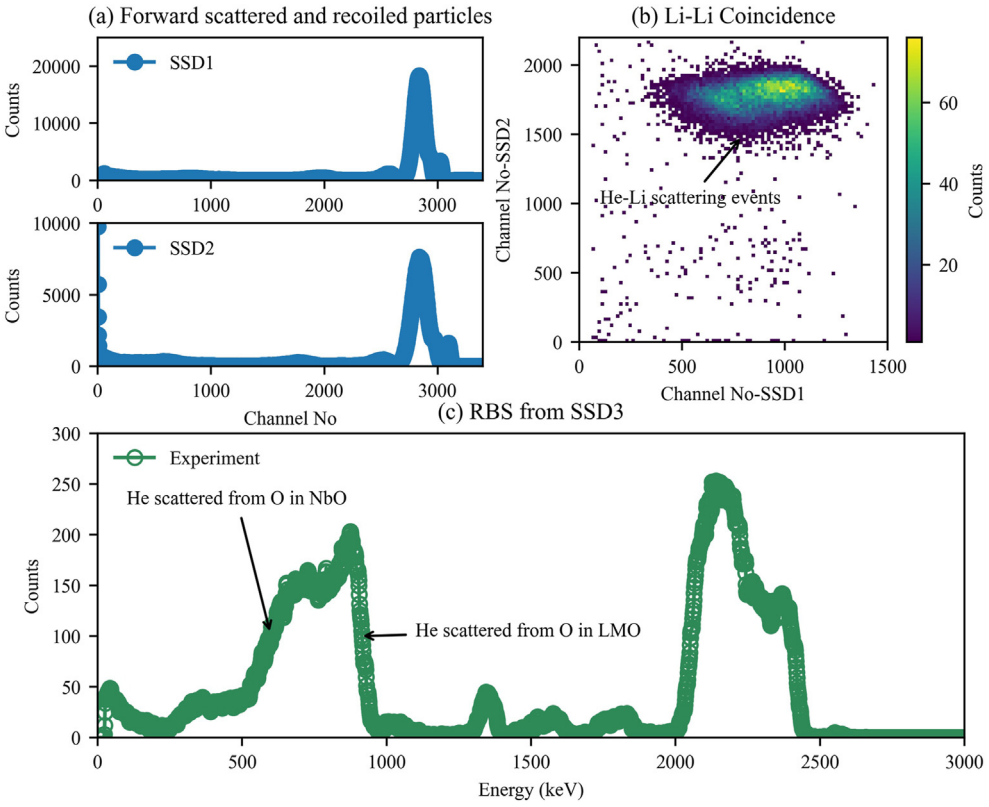

Fig. 5. (a) Experimental spectra of forward scattered/recoiled particles from the battery by 8 MeV He^{2+} ions. (b) He—Li coincidence ERDA spectra of forward scattered/recoiled particles from SSD1 and SSD2. (c) RBS spectra measured simultaneously from the battery for O depth profiling.

of the TFB are found close to Ti(50 nm)/Nb_2O_5(90 nm)/$Li_3PO_{4-x}N_x$(940 nm)/$LiMn_2O_4$(560 nm)/Ti(2 μm).

Fig. 3(a) shows the experimental and simulated spectra of forward scattered and recoiled particles from the three SSDs in a coincidence ERDA experiment using 10 MeV $^7Li^{2+}$ ions. The resulting coincidence ERDA spectrum of Li—Li coincidence is shown in Fig. 3(b). To compensate for effects from small deviations from scattering/recoiling by 45°, the energy of SSD1 and SSD2 is averaged (E1+E2)/2 and the Li—Li coincidence spectra are projected to average energy. The energy-averaged Li transmission ERDA spectra are shown in Fig. 3(c) along with a simulation normalized for the total Li areal density obtained from NRA. Simultaneously, Li—O coincidence events were also measured and are shown in Fig. 3(d). Normalized simulations of O recoils are shown in Fig. 3(e) along with the experiment. However, the concentration of O in the NbO layer was found to be lower than the results from RBS which is attributed to losses due to multiple scattering effects. In addition, the observed difference between experiment and simulation at lower energies is attributed due to intensity losses due to multiple scattering.

Coincidence ERDA was also performed by 10 MeV $^4He^{2+}$ primary ions for comparison. Again, the experimental and simulated transmission ERDA spectra from the three SSDs are shown in Fig. 4 (a). The coincidence ERDA spectrum is shown in Fig. 4(b). The spectrum has a well-separated He—Li coincidence signal. The He—Li coincidence ERDA spectrum shown in Fig. 4(b) is projected on the X-axis, and the recoiled Li spectrum is obtained and shown in Fig. 4(c). Again, the coincidence spectrum was normalized using NRA data for the areal density of Li, and experimental Li depth distribution is simulated using SIMNRA. The composition of Li was adjusted in all the layers, and the optimized simulated Li signal is shown in Fig. 4(c). Simultaneously, He—O coincidence events are also measured (shown in Fig. 4(d)). The experimental O profile from coincidence spectra and normalized simulations of O recoils are shown in Fig. 4(e). Again, the concentration of O in the NbO layer was found to be lower than the results from RBS. In both experiments, using 10 MeV He and Li ions, the O recoils are severely affected from multiple scattering. From coincidence ERDA methods, the O recoils were observed only from part of the battery. However, one could potentially increase the ion energy to depth profile O from the whole battery stack, on the expense of increased measurement time and/or higher dose rate due to lower scattering cross sections. Clearly, our results show coincidence ERDA can be used for simultaneous depth profiling of O and Li.

Lithium and O depth profiling was also performed using 8 MeV He ions. 8 MeV He ions are sufficiently energetic to observe the O backscattering and He—Li forward scattering from the whole battery stack. Again, the Li depth profile was measured from coincidence ERDA, and simultaneously, the O profile was deduced from an RBS spectrum. Fig. 5(a) and (b) shows the spectra of scattered and recoiled particles in SSD1 and SSD2 and the coincidence spectra. The oxygen profile from the full battery stack is obtained from scattered He from O in the battery (shown in Fig. 5(c)). This combined RBS and coincidence ERDA approach allows thus simultaneous depth profiling of Li and O from the whole battery stack with high depth resolution. From RESOLNRA simulations [24], the achievable depth resolution is calculated for He—Li coincidence ERDA and RBS using 8 MeV He ions. A depth resolution of 300 and 720 × 10^{15} atoms/cm^2 was found for Li and O, respectively. From coincidence ERDA using 10 MeV He and Li ions, the achievable depth resolution is 320 and 525 × 10^{15} atoms/cm^2, respectively, for Li. However, very good depth resolution of 85 and 110 × 10^{15} atoms/

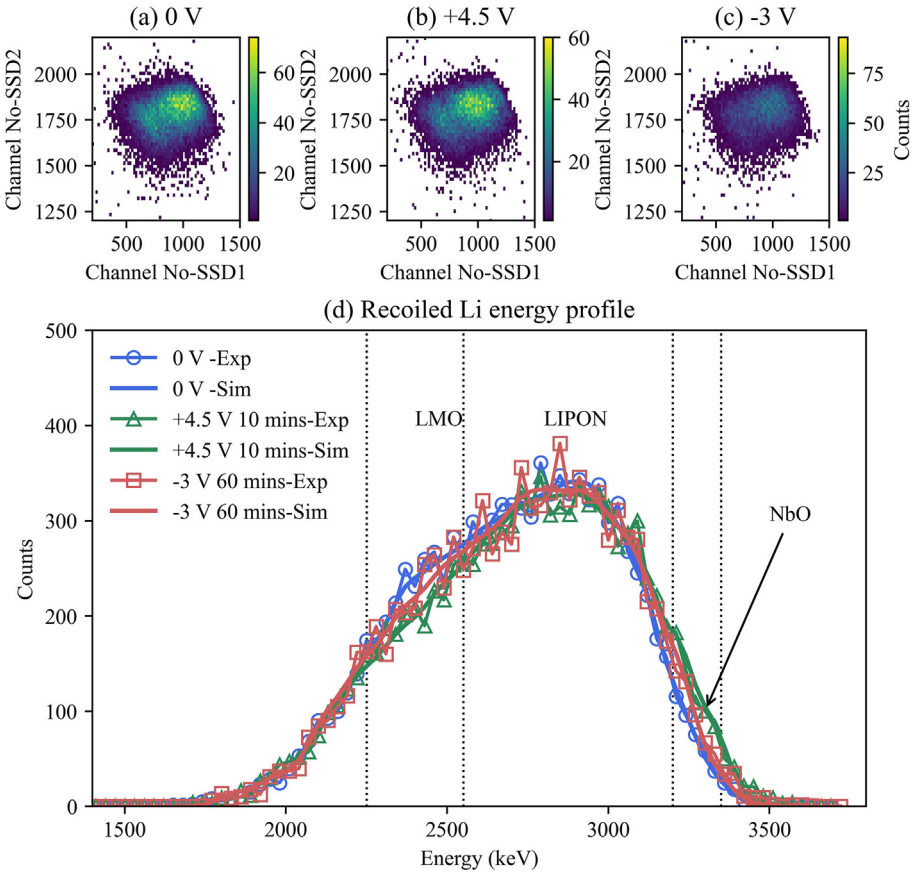

Fig. 6. (a)–(c) Coincidence spectra measured from the battery with 0 V, +4.5 V for 10 min, and −3 V for 60 min. (d) Experimental and simulated Li recoils for 0 V, +4.5 V for 10 min, and −3 V for 60 min.

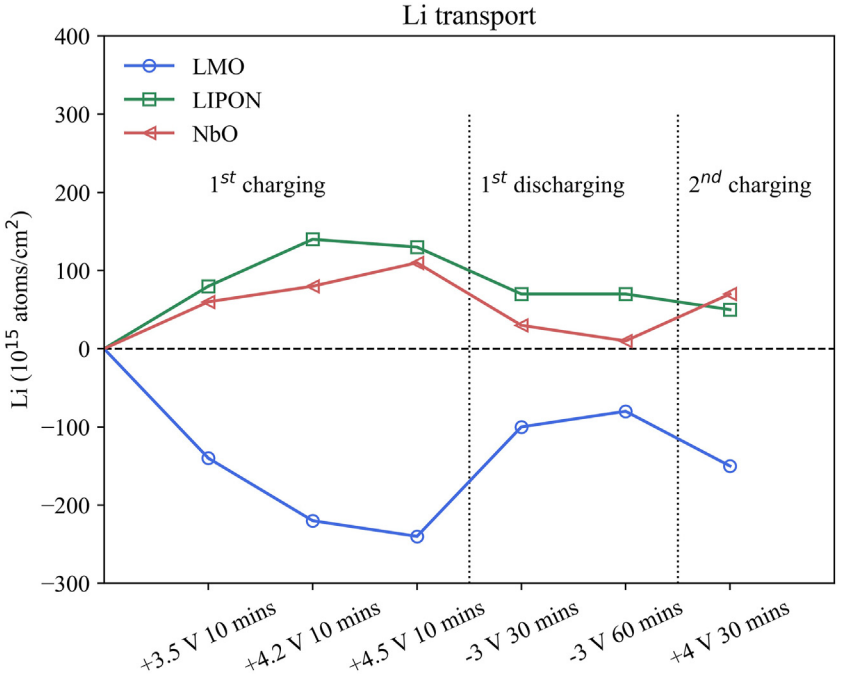

Fig. 7. Quantitative measurements of Li transport in NbO, LMO, and LIPON layers on first charging, first discharging, and second charging.

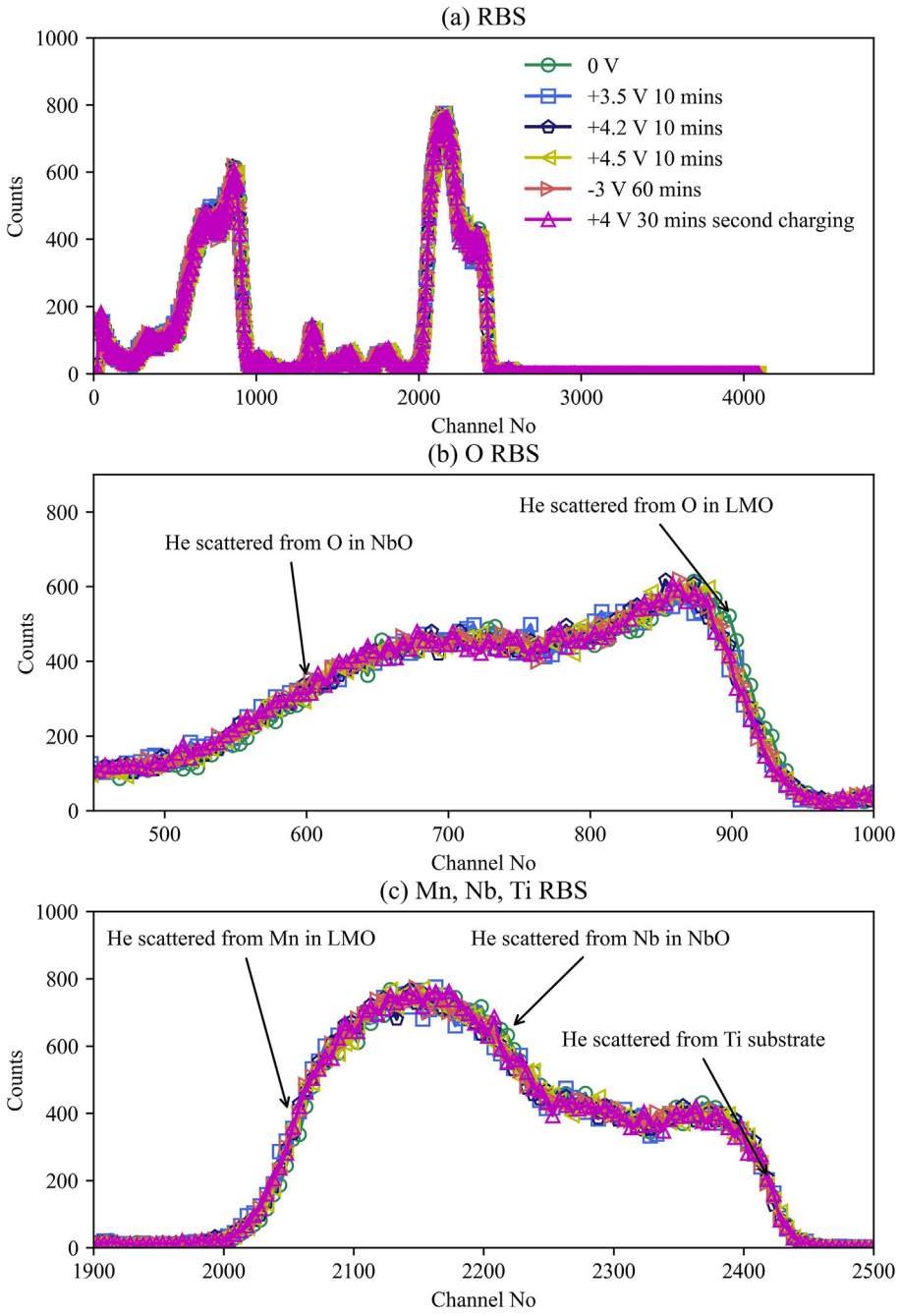

Fig. 8. RBS spectra from the pristine battery and during charging with +3.5 V, +4.2 V, and +4.5 V for 10 min. RBS spectra measured during discharging and second charging also included for comparison. Enlarged RBS spectra from O in the battery and enlarged spectra from Ti, Nb, and Mn scattering are shown in (b) and (c), respectively.

cm^2 was found for recoiled O from coincidence ERDA using 10 MeV Li and He ions, respectively.

The battery was charged in situ by applying a bias of +3.5, +4.2, and +4.5 V for 10 min, and the Li and O profile was measured in each step of charging to study Li and O transport. The He−Li coincidence spectra and the corresponding energy profile of recoiled Li are shown in Fig. 6(a)–(c) along with simulations. From the experimental Li energy spectrum, one can understand the Li transport from LMO to NbO on charging and vice versa on discharging. Energy spectra are simulated using SIMNRA7.02 by assuming a multilayer sample model, and the Li concentration in the sample model was adjusted until a good fit is achieved. The Li depth profile from the fitted sample model is extracted for each measurement, and the quantitative difference in the Li areal density was calculated for the LMO, LIPON, and NbO layers. The Li transport determined for first charging with different voltages, discharging at −3 V with different time, and the second charging with +4 V is visualized in Fig. 7. One can see that this method is very sensitive to the Li loading close to or in the NbO layer. Simultaneously, RBS measurements were also performed on charging and discharging. The obtained RBS spectra are shown in Fig. 8(a). A zoom-in into the spectral region corresponding to scattering from O is shown in Fig. 8(b). Similar to Li, significant transport of O from LMO to NbO is observed on first charging with +3.5 V. Fig. 8(c)

shows the RBS spectrum from Nb and Mn during charging and discharging of the battery stack. The RBS counts of Mn from LMO (around channel No. 2050) are found increased and RBS counts of Nb from NbO (around channel No. 2210) decreased on first charging with +3.5 V which further confirm the O transport from LMO to the NbO layer. However, further O transport is not observed on further charging with higher potentials up to 4.5 V and on discharging and second charging. This result thus suggests that significant transport of Li and O ions occurs from LMO to NbO on very first charging. However, unlike Li, the transport of O is not reversible. From combined coincidence ERDA and RBS techniques, the simultaneous migration of Li and O is evident on first charging. The O migration could be due to the O release from the LMO [25]. Dual ion migration might be also possible for these types of anode materials as earlier observed for a $Li_4Ti_5O_{12}$ cathode [26]. The experimentally observed O extraction from the LMO anode may cause voltage fading of the battery [25] and affect charge-discharge cycles [26]. A low efficiency of 10–16% has been observed in a similar LMO/LiPON/NbO battery stack in the first charge–discharge cycle [18] which could be attributed to the irreversible O transport from LMO to NbO reported here on first charging. Furthermore, also H impurities, introduced during the sample preparation, may be transported from the LMO anode to the NbO cathode on first charging in the battery [19]. Our in-operando ion beam method provides sensitive observation of Li and other light element (H, N, O, S) transport through the battery layers and could thus be used for detailed in-operando studies of voltage fading, capacity fading, and battery degradation in TFBs.

4. Summary and conclusions

Simultaneous depth profiling of Li and O was demonstrated in TFBs by coincidence ERDA experiments using 10 MeV Li and He ions. The Li and O transport was furthermore measured in operando using combined coincidence ERDA and RBS measurements in the battery. Simultaneous transport of both Li and O from the LMO anode to the NbO cathode was observed on first charging with 3.5 V. No detectable O transport was observed on further charging and discharging of the battery stack, whereas reversible transport was observed for Li in repeated charge–discharge cycles. Our in-operando measurements provide direct measurements of Li and O with very good depth resolution and high sensitivity, suitable for ultrathin batteries with a few μm thicknesses.

CRediT author statement

Vairavel Mathayan: Conceptualization; Formal analysis; Investigation; Writing – original draft; Writing – review & editing. **Kenji Morita:** Formal analysis; Project administration; Resources; Validation; Writing – review & editing. **Bun Tsuchiya:** Formal analysis; Resources; Validation; Writing – review & editing. **Rongbin Ye:** Formal analysis; Resources; Validation; Writing – review & editing. **Mamoru Baba:** Formal analysis; Resources; Validation; Writing – review & editing. **Daniel Primetzhofer:** Conceptualization; Formal analysis; Funding acquisition; Project administration; Resources; Supervision; Validation; Writing – review & editing.

Funding

Accelerator operation was supported by Swedish Research Council VR-RFI (Contract No. 2017-00646_9 & 2019-00191) and the Swedish Foundation for Strategic Research (Contract No. RIF14-0053).

Declaration of competing interest

The authors declare that they have no known competing financial interests or personal relationships that could have appeared to influence the work reported in this article.

References

[1] A. Varzi, R. Raccichini, S. Passerini, B. Scrosati, Challenges and prospects of the role of solid electrolytes in the revitalization of lithium metal batteries, J. Mater. Chem. A 4 (2016) 17251–17259, https://doi.org/10.1039/C6TA07384K.
[2] P.G. Balakrishnan, R. Ramesh, T.P. Kumar, Safety mechanisms in lithium-ion batteries, J. Power Sources 155 (2006) 401–414, https://doi.org/10.1016/j.jpowsour.2005.12.002.
[3] P. Bonnick, K. Niitani, M. Nose, K. Suto, T.S. Arthur, J. Muldoon, A high performance all solid state lithium sulfur battery with lithium thiophosphate solid electrolyte, J. Mater. Chem. A 7 (2019) 24173–24179, https://doi.org/10.1039/C9TA06971B.
[4] J. Li, C. Ma, M. Chi, C. Liang, N.J. Dudney, Solid electrolyte: the key for high-voltage lithium batteries, Adv. Energy Mater. 5 (2015) 1401408, https://doi.org/10.1002/aenm.201401408.
[5] C. Huang, C. Lun, A.L.P. Leung, P.S. Grant, A solid-state battery cathode with a polymer composite electrolyte and low tortuosity microstructure by directional freezing and polymerization, Adv. Energy Mater. 11 (2021) 2002387, https://doi.org/10.1002/aenm.202002387.
[6] J. Schnell, F. Tietz, C. Singer, A. Hofer, N. Billot, G. Reinhart, Prospects of production technologies and manufacturing costs of oxide-based all-solid-state lithium batteries, Energy Environ. Sci. 12 (2019) 1818–1833, https://doi.org/10.1039/C8EE02692K.
[7] Y. Ren, K. Chen, R. Chen, T. Liu, Y. Zhang, C.-W. Nan, Oxide electrolytes for lithium batteries, J. Am. Ceram. Soc. 98 (2015) 3603–3623, https://doi.org/10.1111/jace.13844.
[8] M. Balaish, J.C. Gonzalez-Rosillo, K.J. Kim, Y. Zhu, Z.D. Hood, J.L.M. Rupp, Processing thin but robust electrolytes for solid-state batteries, Nat. Energy 6 (2021) 227–239, https://doi.org/10.1038/s41560-020-00759-5.
[9] Z. Qu, M. Zhu, H. Tang, L. Liu, Y. Li, O.G. Schmidt, Towards high-performance microscale batteries: configurations and optimization of electrode materials by in-situ analytical platforms, Energy Storage Mater 29 (2020) 17–41, https://doi.org/10.1016/j.ensm.2020.03.025.
[10] C.J. Jafta, S. Prévost, H. Lilin, L. Mengya, S. Xiao-Guang, Y. Guang, I. Belharouak, J. Nanda, Quantifying the chemical, electrochemical heterogeneity, and spatial distribution of (poly) sulfide species using Operando SANS, Energy Storage Mater 40 (2021) 219–228, https://doi.org/10.1016/j.ensm.2021.05.016.
[11] I. Tomandl, J. Vacik, T. Kobayashi, Y.M. Sierra, V. Hnatowicz, V. Lavreniev, P. Horak, G. Ceccio, A. Cannavo, M. Baba, R. Ye, Analysis of Li distribution in ultrathin all solid-state Li-ion battery (ASSLiB) by neutron depth profiling (NDP), Radiat. Eff, Defects Solids 175 (2020) 394–405, https://doi.org/10.1080/10420150.2019.1701471.
[12] S. Surblé, C. Paireau, J.-F. Martin, V. Tarnopolskiy, M. Gauthier, H. Khodja, L. Daniel, S. Patoux, Operando analysis of lithium profiles in Li-ion batteries using nuclear microanalysis, J. Power Sources 393 (2018) 37–42, https://doi.org/10.1016/j.jpowsour.2018.05.027.
[13] Y. Sunitha, S. Kumar, Depth profiling Li in electrode materials of lithium ion battery by $^{7}Li(p,\gamma)^{8}Be$ and $^{7}Li(p,\alpha)^{4}He$ nuclear reactions, Nucl. Instrum. Methods B 400 (2017) 22–30, https://doi.org/10.1016/j.nimb.2017.03.141.
[14] B. Tsuchiya, K. Morita, S. Nagata, T. Kato, Y. Iriyama, H. Tsuchida, T. Majima, Dynamic measurements of Li depth profiles in a Li-ion battery system under charging condition by means of ERD and RBS techniques, Surf. Interface Anal. 46 (2014) 1187–1191, https://doi.org/10.1002/sia.5620.
[15] B. Tsuchiya, J. Ohnishi, Y. Sasaki, T. Yamamoto, Y. Yamamoto, M. Motoyama, Y. Iriyama, K. Morita, In situ direct lithium distribution analysis around interfaces in an all-solid-state rechargeable lithium battery by combined ion-beam method, Adv. Mater. Interfaces 6 (2019) 1900100, https://doi.org/10.1002/admi.201900100.
[16] K. Morita, B. Tsuchiya, H. Tsuchida, T. Majima, High resolution Li depth profiling of solid state Li ion battery by TERD technique with high energy light ions, Solid State Ionics 344 (2020) 115135, https://doi.org/10.1016/j.nimb.2018.04.003.
[17] V. Mathayan, M.V. Moro, K. Morita, B. Tsuchiya, R. Ye, M. Baba, D. Primetzhofer, In-operando observation of Li depth distribution and Li transport in thin film Li ion batteries, Appl. Phys. Lett. 117 (2020), 023902, https://doi.org/10.1063/5.0014761.
[18] R. Ye, K. Ohta, M. Baba, Electrochemical properties of amorphous Nb2O5 thin film and its application to rechargeable thin film lithium ion batteries, ECS Trans 73 (2016) 49. https://iopscience.iop.org/article/10.1149/07301.0049ecst/meta.
[19] K. Morita, B. Tsuchiya, R. Ye, H. Tsuchida, T. Majima, In-situ total Li depth profiling of solid state Li ion batteries under charging and discharging by means of transmission elastic recoil detection analysis with 5 MeV He^{2+} ions, Nucl. Instrum. Methods B 479 (2020) 249–253, https://doi.org/10.1016/j.nimb.2020.07.018.

[20] M. Mayer, SIMNRA, a simulation program for the analysis of NRA, RBS and ERDA, AIP Conference Proceedings 475 (1999) 541, https://doi.org/10.1063/1.59188.
[21] Y. Serruys, J. Tirira, P. Trocellier, Forward Recoil Spectrometry, Springer US, 1996. https://link.springer.com/book/10.1007/978-1-4613-0353-4.
[22] H.C. Hofsäss, N.R. Parikh, M.L. Swanson, W.K. Chu, Elastic recoil coincidence spectroscopy (ERCS), Nucl. Instrum. Methods B 58 (1991) 49–70, https://doi.org/10.1016/0168-583X(91)95678-7.
[23] J. Mayer, E. Rimini, Ion Beam Handbook for Material Analysis, Academic Press, New York, San Francisco, London, 1977.
[24] M. Mayer, RESOLNRA: a new program for optimizing the achievable depth resolution of ion beam analysis methods, Nucl. Instrum. Methods B 266 (2008) 1852–1857, https://doi.org/10.1016/j.nimb.2007.11.071.
[25] E. Hu, X. Yu, R. Lin, X. Bi, J. Lu, S. Bak, K.-W. Nam, H.L. Xin, C. Jaye, D.A. Fischer, K. Amine, X.-Q. Yang, Evolution of redox couples in Li- and Mn-rich cathode materials and mitigation of voltage fade by reducing oxygen release, Nat. Energy 3 (2018) 690–698, https://doi.org/10.1038/s41560-018-0207-z.
[26] F.Q. Meng, Q.H. Zhang, A. Gao, X.Z. Liu, J.N. Zhang, S.Y. Peng, X. Lu, L. Gu, H. Li, Synergistic O2−/Li+ dual ion transportation at atomic scale, Research 2019 (2019) 9087386, https://doi.org/10.34133/2019/9087386.